Journal of the Optical Society of America A
OPTICS, IMAGE SCIENCE, AND VISION

Rendering spectral images

MARK GESLEY* AND ROMIN PURI

Spynsite LLC, Oakland, California 94610-5005, USA
*Corresponding author: gesley@spynsite.com

Received 19 July 2022; revised 26 September 2022; accepted 27 September 2022; posted 28 September 2022; published 21 October 2022

Objects of interest are rendered from spectral images. Seven types of blood and cancer cells are imaged in a microscope with changes in source illumination and sensor gain over one year calibrated. Chromatic distortion is measured and corrections analyzed. Background is discriminated with binary decisions generated from a training sample pair. A filter is derived from two sample-dependent binary decision parameters: a linear discriminant and a minimum error bias. Excluded middle decisions eliminate order-dependent errors. A global bias maximizes the number and size of spectral objects. Sample size and dimensional limits on accuracy are described using a covariance stability relation.

https://doi.org/10.1364/JOSAA.470814

1. INTRODUCTION

A spectral image microscope illuminates a sample substrate with visible light sequentially passed as narrow bands by a monochromator. The detected output is a sequence of gray images over a wavelength range of 440–620 [nm] with ∼10 [nm] channel bandwidth. A sequential series of the field of view (FOV) is assembled as a frame array of pixelized intensity vectors (Fig. 1). Blood and cancer cells are imaged as spectral objects from thin films on glass slides using a prototype transmission optic at near-diffraction-limited resolution with 0.4 [μm] pixels [1]. As part of a high throughput system architecture, electronic noise and compute platform requirements were evaluated and chromatic distortion image contrast effects shown, but no discrimination or rendering methods were evaluated. An overview of spectral object classification with an application for label-free blood and cancer cell identification used four cell types [2]. In neither of these studies were calibration methods evaluated.

This paper describes how to render objects of interest and compensate for systematic errors. In the seven cases studied here, a slide substrate holds a single population type: erythrocyte (Rbc) and leukocyte (Wbc) blood cells; epithelial cell lung carcinoma (A549), large cell lung cancer (H460), non-small cell lung cancer (H1975), Jurkat T-lymphocyte cancer (Jur), and B lymphocyte (Ramos) cells. Image signal processing and calibrations for source illumination and sensor gain are described in Section 2. A binary decision filter is constructed to discriminate intensity vectors in Section 3. A global bias maximizes the number and size of cell spectral objects by filtering residual sample artifacts in Section 4. Chromatic distortion correction (CDC) is analyzed in Section 5. Spatial distributions of rendered cells are displayed in Section 6.

2. SPECTRAL IMAGE SIGNAL PROCESSING

Signal processing begins with camera detector output—a monochromatic gray scale 653×492 pixel FOV with 16 (bit/pixel) intensity. A cell population occupies one FOV. Two cameras with field sizes 653(x), 492(y) and 1392(x), 1040(y) were used with a common Xe-arc lamp source and image transfer optics. The larger field was cropped for comparison. Pixel coordinates (x, y) and measurement vectors $(\hat{\mathbf{x}})$ of detected intensities $\hat{x}_j$ at p dimensions (wavelengths) represent a FOV map. A raw score is the sum of measured intensities $S(\hat{\mathbf{x}}) = \sum_{j=1}^{p} \hat{x}_j$. Transformed score distributions are used to discriminate objects of interest from the background in Section 3.

Bright-field (BF) and dark-field (DF) combinations are used to compensate for source-illumination and sensor-gain variations (Fig. 2). Zeroth-order unscattered light is included in a BF image. The ratio of dark and bright FOVs is determined by zeroth-order beam filtering [1]. The system is calibrated with two parameters: an offset of at least one pixel with zero intensity in the DF (input 1) and an intensity scale to align the BF average source intensity scores ⟨BFscore⟩ (input 2). Scores are normalized to 110,000, setting a scaled intensity of 1000 for $p = 11$ dimensions. The Jurkat (Jur) case also corrected a 5% raw intensity gain error. Score statistics for microscope operation over one year are shown in Table 1 with the normalized distributions for seven samples. The two signal parameter inputs align the scaled BF score distributions (left) and scaled offset DF score distributions (right) in Fig. 3.

3. BACKGROUND DISCRIMINATION

Discrimination identifies and separates one population from another. Background discrimination removes regions of non-interest from a FOV. A discrimination classifier is constructed

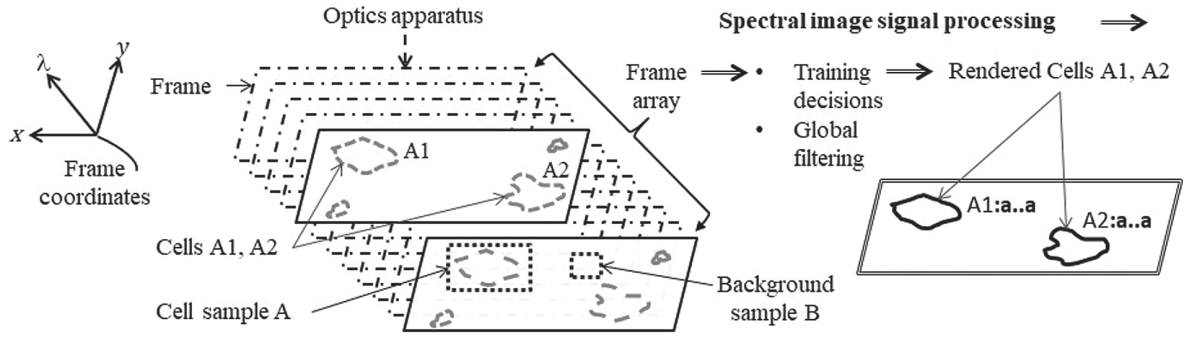

Fig. 1. Series of grayscale field of view frames are illuminated over a range of wavelengths. Training sample binary decisions discriminate background. Global bias compensates for non-sample related errors. Cell spectral objects are rendered by pixel sorting of filtered intensity vectors.

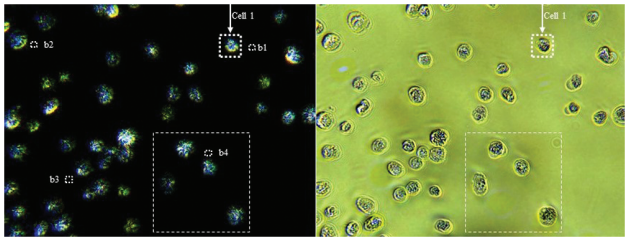

Fig. 2. A549 cell population displayed in dark (left) and bright (right) fields as RGB images: red (620 [nm]), green (530 [nm]), and blue (440 [nm]). A sample box encloses cell1 (A = X0) and background $b1b2b3b4$ (B = Y0) samples used for training. For scale, the dashed box in the lower right quadrant encloses four cells and 200 × 200 [pixels].

that transforms input vectors with iterative filtering. Samples size, dimensionality, and heterogeneity are evaluated with binary decisions derived from a training set pair: a feature of interest A enclosing all or a portion of a cell and a background region B. A sample object of interest is selected based on some knowledge, e.g., morphology or origin from a cell line [3]. A sample is specified by a cell-type set-label as knowledge separate from algorithmic actions, e.g., transfer of a class label to member vectors. A training class sample set pair of vectors $\hat{\mathbf{x}}_A = [\hat{x}_1, \cdots \hat{x}_p]_A$ and $\hat{\mathbf{x}}_B = [\hat{x}_1, \cdots \hat{x}_p]_B$ is transformed to maximize their mean separation to joint variance [4]. A linear approximation to the maximized sample statistics produces a scale vector:

$$\lambda_{AB} = [\lambda_1, \cdots \lambda_p]_{AB} = \mathbb{C}^{-1}\langle \hat{\mathbf{x}}_A - \hat{\mathbf{x}}_B \rangle, \tag{1}$$

with linear discriminants (λ_j), within-class variations ($\hat{\delta}x_j = \hat{x}_j - \langle x_j \rangle_T$), and a pooled covariance matrix $\mathbb{C} = [C_{jk}] = (\langle \delta x_j \delta x_k \rangle_A + \langle \delta x_j \delta x_k \rangle_B)$ averaged over the training class T sample sets A and B. Vectors are transformed to a dual space score distribution by an inner product with the scale vector

$$D(\hat{\mathbf{x}}) = \lambda \cdot \hat{\mathbf{x}} = \sum_{\mathbf{j}=1}^{\mathbf{p}} \lambda_{\mathbf{j}} \hat{\mathbf{x}}_{\mathbf{j}}, \tag{2}$$

Table 1. Score Distribution Statistics for Seven Cell Types[a]

		Bright Field (BF)				Dark Field (DF)								
Upper Left (UL) FOV 653 × 492 Cell Type		Max BF Score	⟨BF Score⟩	⟨Scaled BF Score⟩	Scaled BF FOV Score	DF Max. Score	DF Min. Score	Max Scaled DF Score	Min Scaled DF Score	Scaled DF FOV Score	DF/BF Intensity	Input 1 Intensity Offset DF	Input 2 Scale Gain BF
UL					3.534E + 10			49,658	77	4.128E + 08	1.2%	10	76.9
	A549	2,495	1,431	110,000		756	111						
UL					3.533E + 10			53,378	618	5.139E − K58	1.5%	10	77.2
	H460	2,443	1,424	110,000		801	118						
UL					3.533E + 10			59,462	0	4.290E + 08	1.2%	10	79.0
	HI 975	2,639	1,393	110,000		863	110						
UL					3.534E + 10			112,538	324	6.517E − H58	1.8%	29	0.2
	Ramos	654,072	441,971	110,000		452,489	1,619						
					3.375E + 10			190,202	412	3.709E + 08	1.1%	0	1.9
	Jur	96,551	55.839	105,036		*101,114*	219						
					3.534E + 10			61,959	1,181	1.262E + 09	3.6%	248	1.1
	Rbc	189,133	103,944	110,000		61,276	3,844						
					3.534E + 10			168,150	27	4.005E + 08	1.1%	0	2.3
	Wbc	96,925	48,432	110,000		74,035	12						

[a]Dark-field (DF) sensor offsets (input 1) and gains are adjusted based on the BF score averages (input 2).

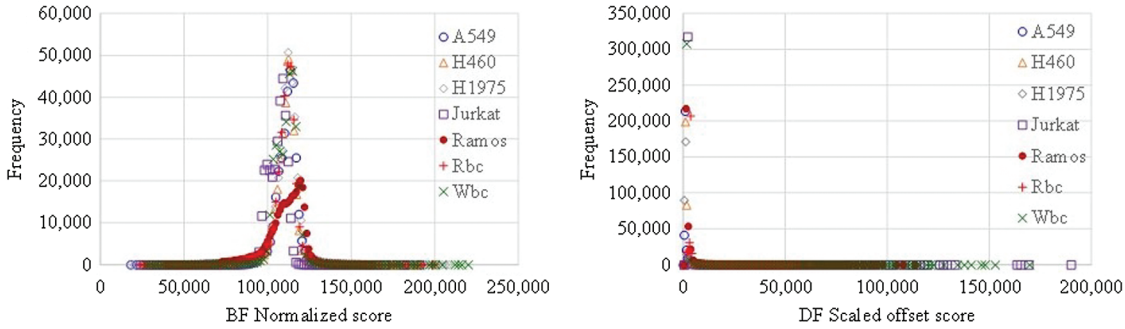

Fig. 3. Histograms for seven blood types: (left) bright-field (BF) scores aligned with the Table 1 scale gain (input 2); (right) dark-field (DF) scores adjusted with the offset and scale parameters (inputs 1 and 2).

where p is measurement dimensions and λ a weight or linear functional, depending on the context.

A generic binary decision is typically defined as a conditional statement that associates one outcome, labeled $(:a)$ if $f(\hat{\mathbf{x}}) \geq h$, for a functionally transformed input vector compared to a scalar threshold-bias value h, labeled $(:b)$ otherwise if $f(\hat{\mathbf{x}}) < h$. Decisions with two independent parameters—a generalized weight vector and threshold-bias scalar—are commonly used. The perceptron is an iterative linear decision process that evaluates an inner product $f(\hat{\mathbf{x}}) = \mathbf{w} \cdot \hat{\mathbf{x}}$ with a weight vector $\mathbf{w}$ and a sample vector $\hat{\mathbf{x}}$ [5]. However, convergence is not guaranteed [6], and iteratively specifying a weight vector and bias does not necessarily yield a unique solution as sample order can create several outputs [7]. Support vector machines use nonlinear transformations to generate a score distribution with a binary decision: if $K(w, \hat{\mathbf{x}}) \geq h$, associate $\hat{\mathbf{x}}$ with label a $(\hat{\mathbf{x}} : a)$, else $(\hat{\mathbf{x}} : b)$ for a kernel operator $K(\mathbf{w}, \hat{\mathbf{x}})$ [6]. Networks of binary decisions use weighted vector transformations and biases [8]; however, an architecture can be difficult to find or obscure insight to an underlying process [9–11].

In this paper, binary decisions are constructed from two sample dependent parameters: the scale vector λ_{AB} of Eq. (1) and a minimum error bias. Sample independent nonlinear transformations and network heuristics are avoided. Sample sets of vectors $\{\hat{\mathbf{x}}_A\}$ and $\{\hat{\mathbf{x}}_B\}$ generate Eq. (1), and are transformed by Eq. (2) to dual score distributions $D_0(\hat{\mathbf{x}}_\mathbf{A}) = \lambda_{AB} \cdot \hat{\mathbf{x}}_A$ and $D_0(\hat{\mathbf{x}}_\mathbf{B}) = \lambda_{AB} \cdot \hat{\mathbf{x}}_B$, e.g., Fig. 4 (left). A training vector $\hat{\mathbf{x}}$, sampled from set A class, is assigned a binary decision $(a :)$, noted as $(\hat{\mathbf{x}} : a : A)$. The ⟨decision : class⟩ equivalence relation is defined as $\langle a : A \rangle = \text{true}$, and thus, $\langle b : B \rangle = \text{true}$, $\langle a : B \rangle = \text{false}$, and $\langle b : A \rangle = \text{false}$. Errors are defined by false binary decisions. In general, there is no prior knowledge about the truth of a ⟨decision : class⟩ equivalence, e.g., $\langle a : B \rangle = \text{true}$ could also be assumed. A logical equivalence may be determined in some fields if a relation is known. Here it is not required that a particular boolean equivalence relation be established. Both types of decisions are evaluated to find a minimum error bias. To cover both situations, a bias $(b_\pm)$ is denoted with $\pm$ to indicate the inequality $(<)$ or $(>)$ used. Total error and false condition distributions are related by

$$\epsilon(b_\pm) = n(b : A) + n(a : B), \tag{3}$$

where $n(b : A)$ and $n(a : B)$ are numbers of false decisions at bias $(b_\pm)$. Thus, all training set pair A, B vectors are associated with boolean true or false values and generate error distributions, as shown in Fig. 4 (right).

Set size biases a decision, particularly if samples differ by a relatively large amount. Score histograms shown thus far have an assigned value of one for each event so that a sum of events equals a set size. As there is no prior knowledge, both large and small set sizes are assumed equally important, and a size-bias correction is made where a decision outcome of a member of set $\hat{\mathbf{x}} \in S$ is assigned a value $1/n(S)$. By normalizing values, a sum over a training set density equals one. The normalized total error distribution shown in Fig. 5 (left) corresponds to the training sample pair $(A0,\ B0)$ in Fig. 4.

A minimum error can always be found as Eq. (3) yields convex and concave distributions for the two decision types. However, the magnified scale of Fig. 5 (right) reveals a discontinuity at the minimum normalized error bias $h = b_{+0} = 176.114$. The nature of this discontinuity is understood by evaluating the generic decisions for the training class pair A, B, which as shown in Fig. 6 produces $n(\text{FN}) = 413$ false negatives and $n(\text{FP}) = 26$ false positives.

In this work, decisions use commutative set-pair A and B operations and are independent of set member ordering. A portion of the generic binary decision expression is retained: if $D(\hat{\mathbf{x}}) > h$, assign a labeled decision as $(\hat{\mathbf{x}} : a)$, and if $D(\hat{\mathbf{x}}) < h$, $(\hat{\mathbf{x}} : b)$. However, the special case of $D(\hat{\mathbf{x}}) = h$ must be analyzed separately, as a multiset of vectors at the minimum error bias creates order-dependent minimum error counting. To see this, sort the dual scores in an ascending series and index the multiset members. The minimum normalized error corresponds to the bias $h = b_{+0} = 176.114$. While the multiset shares the same score h, indicial permutations result in multiple minimum error estimates. An upper limit to the number of variations corresponds to the multiplicity of vectors in the multiset. Under these conditions, the generic decision must be modified to avoid an order-dependent error result.

Order-dependent errors are avoided by filtering of all vectors in the multiset using the logic if $D(\hat{\mathbf{x}}) = h$, and $\hat{\mathbf{x}} \in A$ then $\langle \hat{\mathbf{x}} : b \rangle$; or if $\hat{\mathbf{x}} \in B$ then $\langle \hat{\mathbf{x}} : a \rangle$. The implication is if $D(\hat{\mathbf{x}}) = h$, then $\hat{\mathbf{x}}$: False. The consequence is that false outcomes increase to a total of 641 when the excluded middle decision is executed (Fig. 7). The figure also identifies the multiplicity $m(h) = 202$ with the size of the discontinuity shown in

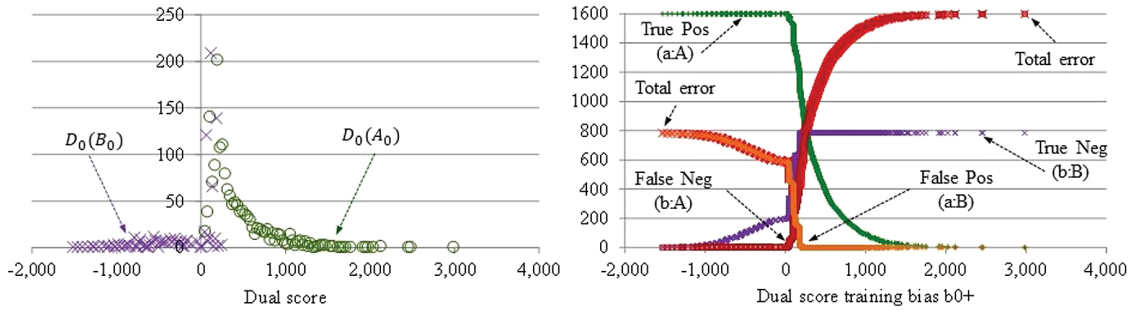

Fig. 4. Training sample pair DF score distributions: H460 cell25 in $D_0(X_0 = A_0)$ and background $D_0(Y_0 = B_0)$ (left); corresponding error distributions (right). Set sizes are $n(A_0) = 1600$ and $n(B_0) = 784$ with class labels A(Positive) and B(Negative).

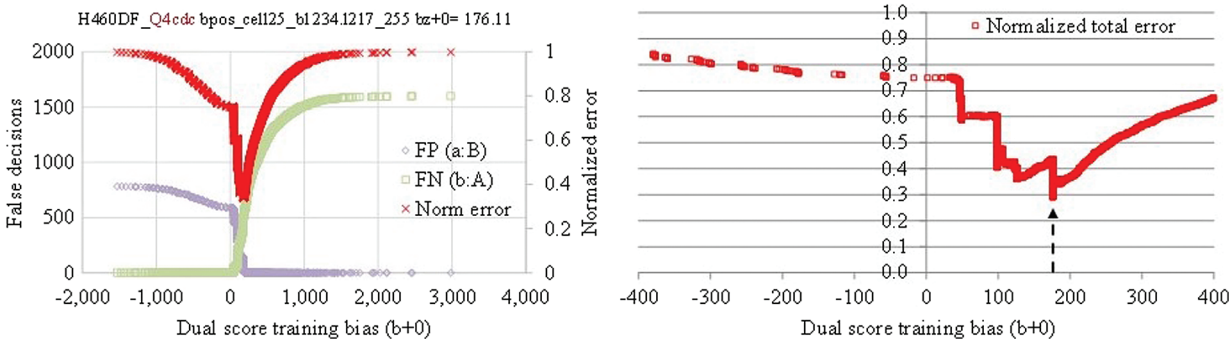

Fig. 5. Normalized total error distribution for the training sample dual scores of Fig. 4 (left); the magnified range reveals a discontinuity at the score bias $b_{0+} = 176.114$ (dashed arrow) due to a multiplicity of vectors (right).

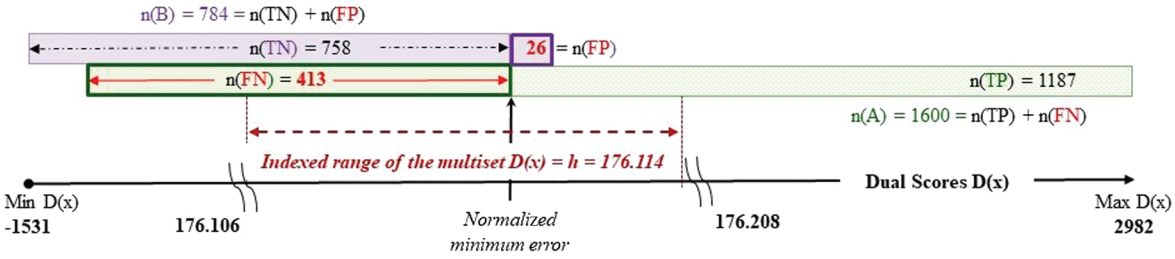

Fig. 6. Generic binary decision: if $D(x) > h$, then label $x : a$; else if $D(x) \leq h$, label $x : b$. Scores sorted in a monotonic non-decreasing order left to right correspond to Fig. 5.

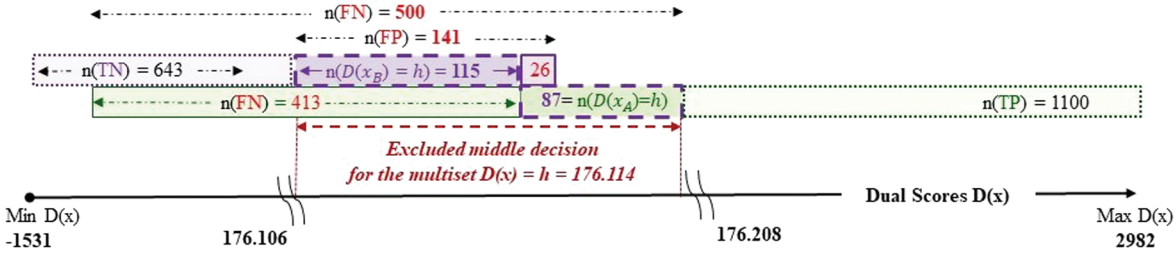

Fig. 7. Excluded middle decision: If $D(x) = h$, then label x:False. The multiplicity $m(h) = 202$ is the number of additional false decisions in the multiset beyond those identified by the generic decision (purple dashed intervals).

Fig. 5 (right). This resolves the ambiguity of a generic binary decision by using an excluded middle decision constructed from two sample-dependent parameters: the linear scale vector λ_{AB} of Eq. (2) and the minimum error bias h.

Mixed populations are iteratively filtered by excluded middle binary decisions. A sieve algorithm operates on an input training sample pair A, B and filters false vectors at the minimum error bias. The sieve iteratively generates two dependent parameters: linear discriminant scale vector [Eq. (1)] and minimum error bias ($h = b_{\pm}$). The unfiltered set of true training class members is input to the next iteration: $\{\hat{x} \in A : a\} = A_1 \subseteq A_0$ and $\{\hat{x} \in B : b\} = B_1 \subseteq B_0$.

Table 2. Binary Decision Ensemble for Training Sample Pair: $D_0(A_0)$, $D_0(B_0)$ in Fig. 4[a]

Iter	Pos/Neg	Minimum Error Bias	Scaled Lambda Vector (H460DF-10 x 77.2_Q4cdc cell25_bl234)										
0	1	176.114	1.0	−0.787	0.039	0.644	0.102	0.041	−0.409	−0.581	0.863	0.571	−0.100
1	1	157.853	1.0	−0.535	−0.280	0.703	0.087	0.097	−0.476	−0.836	1.173	0.568	−0.160
2	1	139.065	1.0	−0.518	−0.344	0.772	0.054	0.138	−0.454	−1.000	1.296	0.585	−0.212
3	1	138.848	1.0	−0.520	−0.341	0.772	0.057	0.139	−0.450	−1.020	1.314	0.583	−0.217

[a]Pos/Neg denotes the decision inequality and relative pair orientation to the dual score minimum error bias.

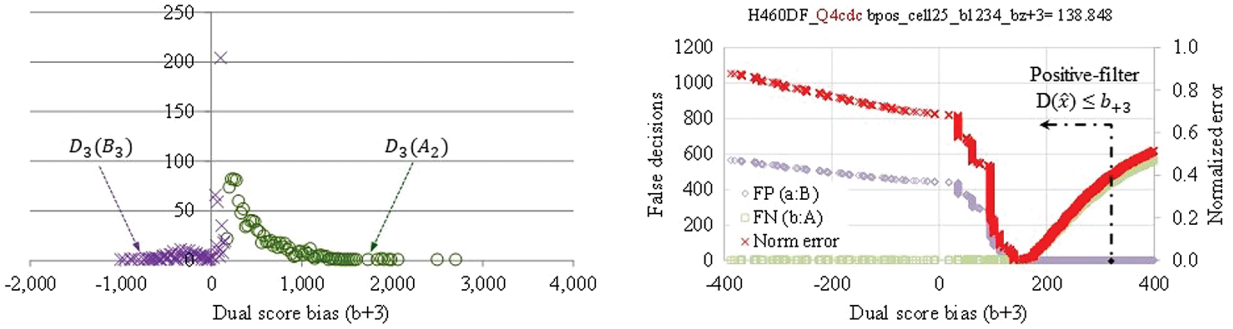

Fig. 8. (Left) Disjoint training pair dual scores for cell25, H460DF − 10x 77.2q4cdc: $D_3(A_2)$ and background $D_3(B_3)$; set sizes are $n(A_2) = 1091$ and $n(B_3) = 634$. (Right) Corresponding false decision distribution with zero error at training bias $b_{z+3} = 139$. A global bias filter at $b_z = 335$ optimizes the number and size of rendered objects in the presence of non-sample related errors (Section 4).

	Class A(Pos)	Class B(Neg)	
Outcome a:	<a:A> TP 1091	<a:B> FP 150	a: predictive value TP/(TP + FP) 88%
Outcome b:	<b:A> FN 509	<b:B> TN 634	b: predictive value TN/(FN + TN) 55%
	Sensitivity TP/(TP+FN) 68%	Specificity TN/(FP+TN) 81%	
Acc = (TP+TN)/(P+N)		72%	
	n(A) 1600	n(B) 784	

Fig. 9. Error components at the final training iteration using excluded middle decisions for the Fig. 8 example.

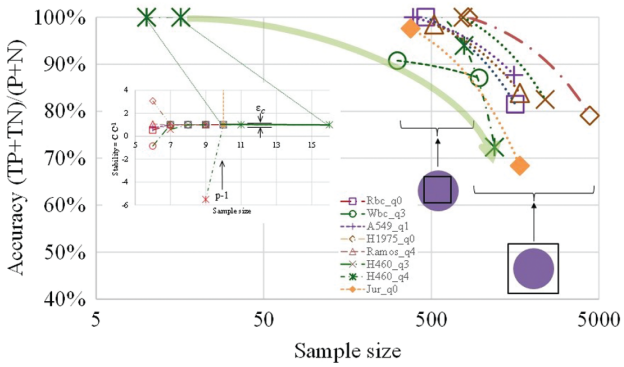

Fig. 10. Sieve accuracy for seven cell types. The inverse relation between accuracy and sample size is highlighted by the broad green arrow: sample (square inscribed in circle) and a larger sample (circle inscribed in square). Inset plots covariance stability with a tolerance ϵ_c. Sample size limits are reduced in some lower (<10) dimensional subspaces.

The algorithm converges to disjoint dual score distributions $\{D(\hat{x} \in A : a)\} \cap \{D(\hat{x} \in B : b)\} = \emptyset$. The result is a binary decision ensemble $BDE(A, B) = \{\lambda_j, b_{\pm j}\}$—a set of scale vectors and minimum error threshold biases, e.g., Table 2 with three iterations. By the final iteration, the remaining samples have disjoint training distributions (Fig. 8, left) with zero false decisions at the minimum error bias $b_{+3} = 138.8$[right]. The result is a sieve accuracy $(\mathrm{TP} + \mathrm{TN})/(n(A) + n(B) = 72\%$ (Fig. 9).

The sieve accuracy tends to increase with decreasing sample size for the seven cell types (Fig. 10). Two convenient sampling methods highlight sample heterogeneity. One is where a sample box encloses an object of interest (square with inscribed circle). The second is a sample contained within an object of interest (circle with inscribed box). The schematic relation between a sampled region (box) and object of interest (circle) is shown for sample sizes of $n = 784$ (sample inscribed by object) and $n = 1192$ (sample containing object). The sample size $n = 784$ yields 94% accuracy, and $n = 1192$ corresponds to the 72% accuracy in Fig. 9. In this example, homogeneity occurs when background is excluded ($n < 784$). Some classifiers use a homogeneous sample from a single class, species, or type to improve decision accuracy, e.g., flowers of an iris species [4], or tissue spectra [12]. Larger samples with greater heterogeneity from included background regions result in lower accuracy.

As sampling becomes sparse, dimensional reduction may be required to avoid an ill-conditioned transformation, although with the potential of diminishing information. The curse of dimensionality [6,10] is characterized in the present work using the Eq. (2) linear functional. The sample size (n) and dimensionality (p) are constrained by the stability of the covariance matrix (appendix Eq. 3 of [2]), restated here:

$$\det \mathbb{C} \cdot \det \mathbb{C}^{-1} \cong 1 \pm \epsilon_c.$$

The tolerance $\epsilon_c \sim 10^{-5}$ is set above the 64 bit floating point numerical precision with 15–17 significant figures, sufficient to detect instabilities for all cases studied here with a minimum detectable difference $\Delta = 10^{-14}$ and a bound on singular values of $\delta = 10^{-9}$.

Dimensional limits become important when analyzing objects of the order of 1–3 μm (4–36 pixels). A bound on sample size $(p-1) \leq n_{\min}$ is determined by covariance stability with one less degree of freedom—mean intensity spectra $\langle I(\lambda_j)\rangle$ and normalized component of the linear scale vector in Table 2. There are two cases (H460q4 and Jur) where $n_{\min} = 10$ (Fig. 10 inset). If sample size is decreased, the covariance dimension can be further reduced, as occurs in five of seven cases: Rbc, Wbc, Ramos, and H1975 ($n^*_{\min} = 7$) and H460q3 ($n^*_{\min} = 8$). For example, the Rbc covariance matrix has four rows and columns of uncorrelated matrix elements (marked by dashed red arrows, Fig. 11, left). The unweighted matrix elements are $C_{jk} = \langle \delta i(\lambda_j) \cdot \delta i(\lambda_k)\rangle$ with $\delta i(\lambda_j) = I(\lambda_j) - \langle I(\lambda_j)\rangle$. The covariance of the relative intensity fluctuations is $R_{jk} = \langle \delta i(\lambda_j) \cdot \delta i(\lambda_k)\rangle / (\langle I(\lambda_j)\rangle \langle I(\lambda_k)\rangle)$, and root relative intensity $c_j = |R_j|^{1/2}$ per λ_j for each cell type (Fig. 11, right). Stable covariances occur in the examples below with $p = 11$ and sample sizes $n > 50$.

4. GLOBAL BIAS OPTIMIZATION

A training sample pair, transformed to a binary decision ensemble BDE(A, B), is used to discriminate background in a FOV. A binary decision operates on a random vector $\hat{\mathbf{x}} \in$ FOV and assigns a label by the excluded middle conditional expression: if $D(\hat{\mathbf{x}}) > h$, assign a labeled decision $(\hat{\mathbf{x}} : a)$; if $D(\hat{\mathbf{x}}) < h$, $(\hat{\mathbf{x}} : b)$; if $D(\hat{\mathbf{x}}) = h$, then $\hat{\mathbf{x}}$: False. Discrimination proceeds by filtering false pixel vectors, but an added assumption is required since random vectors do not have an assigned ⟨class : decision⟩ equivalence relation. A vector is discriminated if associated with the background decision. This means if a labeled decision is $(\hat{\mathbf{x}} : b)$, then $\hat{\mathbf{x}}$: False. Individual objects are rendered from the filtered FOV by identifying gaps in sorted pixel coordinates.

While discrimination is necessary, it is generally not sufficient to maximize the number and size of rendered objects. For example, nonuniformity with clustered objects can occur across a FOV (Fig. 12, left). Figure 10 shows that sieve accuracy can be improved as sample size is reduced—until covariance instability is met. A sample box inscribing an object of interest leads to greater accuracy, but further size reduction results in diminishing returns due to non-sample related errors. So the relative importance of accuracy in the presence of non-training related errors must be determined. This will answer what sample size results in sufficient accuracy for rendering in the presence of non-sample related errors. Stated alternatively, the method

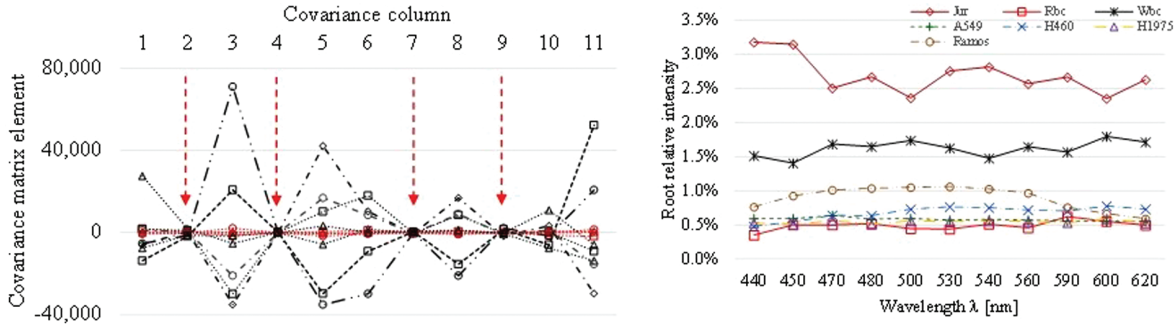

Fig. 11. (Left) Rbc covariance matrix transformed to a seven-dimensional subspace at sample size $n = 7$. This corresponds to the $n = 6$ instability, Fig. 10 inset. This rank deficient symmetric matrix has four null components equal to zero, or so small values are dominated by round off error (red dashed arrows). (Right) Rendered objects root relative intensity $c_j = |R_j|^{1/2}$ per wavelength. *Ref:RbcDF* − 248 × 1.06_ *q0cdcScaledInSpeCoVars7rb7r*.

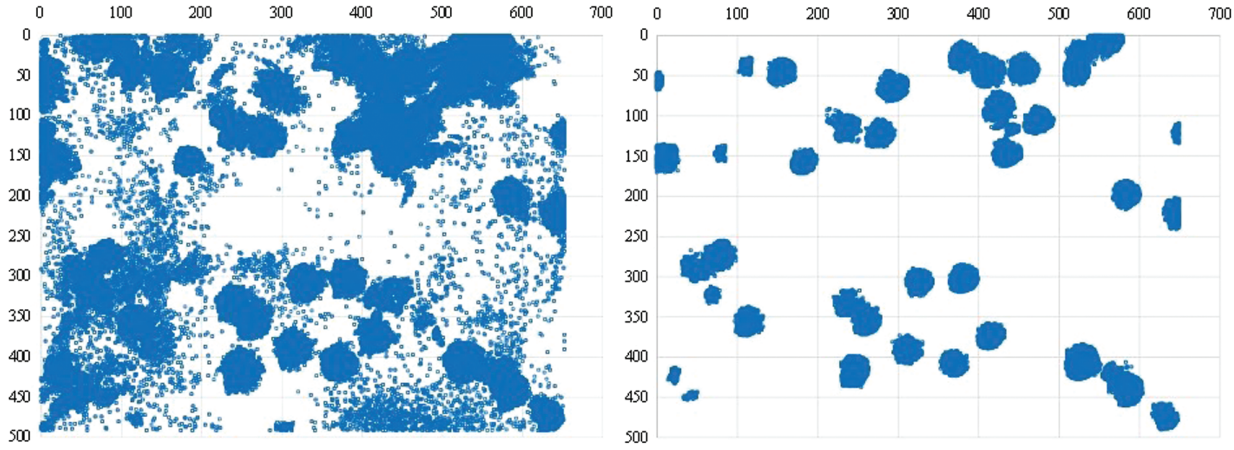

Fig. 12. H460 field of view: (left) discrimination at the minimum error training bias ($b_{+3} = 139$); (right) a global bias ($b_z = 335$) optimizes the Eq. (4) signal and renders 33 objects with sizes $n > 50$ (~3 μm diameter).

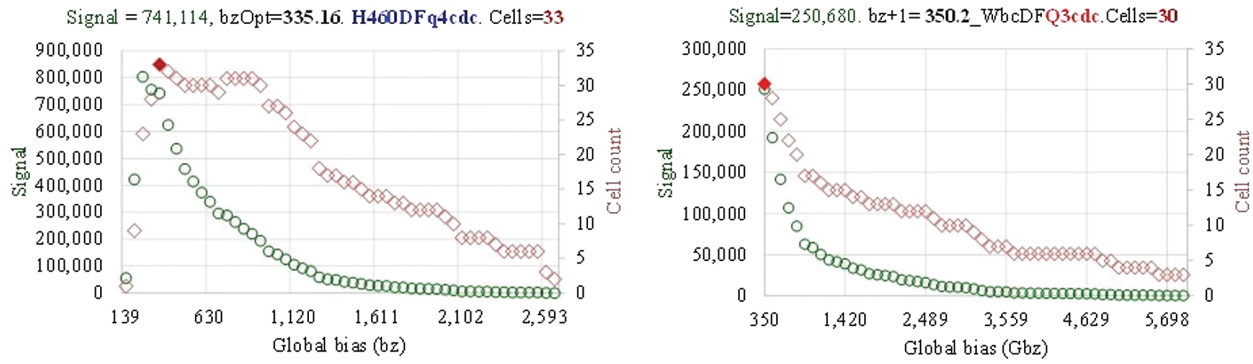

Fig. 13. Global bias filter is required if the signal maximum is not at the dual score minimum error. (Left) Global bias (bzOpt = 335) renders 33 objects, ref : $H460DFq4cdc$. (Right) No global bias is required [training bias (bz + 1 = 350) renders 30 objects, ref : $WbcDFq3cdc$].

answers how binary decision accuracy affects rendered objects when both sample-related and external errors are present.

The solution is to maximize the total number of object pixels. A signal is defined by average object size, and a maximum can be found from the rendered product,

$$\text{Signal} = n(\text{objects}) \times n(\text{object} \cdot \text{pixels}), \quad \textbf{(4)}$$

by adjusting a global bias. A positive-filter of false-decision pixel vectors, the global bias reduces non-sample related errors in the FOV, e.g., global bias $b_z = 335$ in Fig. 8 (right) renders the maximum number of 33 objects in Fig. 13 (left), and results in Fig. 12 (right). From these relations, the object number maximum is found. If multiple global biases with a maximum number of objects occur, the one with the largest signal is chosen. Then [signal/n(object)] is derived, which corresponds to the largest number of object pixels at the maximum object number. As a result, sieve accuracy and number of rendered object pixels are determined, e.g., Fig. 14 normalized maximum corresponds to a 15 μm length scale at 90% accuracy and sample size of $n \sim 900$ from Fig. 10.

5. CHROMATIC DISTORTION CORRECTION

Chromatic distortion is a wavelength-dependent image shift due to sample illumination and objective lens image transfer to the detector. Positional shifts are measured using an extended object to compensate for image contrast changes (Fig. 15). The chromatic distortion is measured in four quadrants for each of three slide substrates using camera A in Fig. 16 (left). The slide–slide variations are greater than the chromatic distortion. In this case, calibrations can be applied only on a per slide basis. With camera B, the lowest distortion area is the upper left (UL) region cropped to match the 653 × 492 pixel field of camera A (Fig. 16, right).

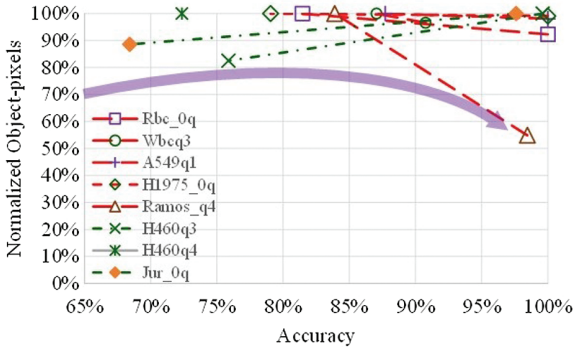

Fig. 14. Sieve training accuracy relation to rendered objects (normalized to cell type maxima). Within a cell type, rendered objects exhibit negative (red solid lines) or positive (dashed green lines) changes with accuracy. Object-pixel maxima reflect training accuracy and global bias effects on rendering.

CDCs are shown in Table 3 for the seven cell types (columns) and by quadrant calibration site (rows), with no CDC correction denoted (0cdc). The pixel shift values in boxes correspond to the maximum rendering per cell type. In cases H1975, Jurkat, Rbc, no correction (light brown boxes) yielded better rendering than calibrations at 1.8, 2.7, 4.1 (yellow box, red font). For A549, H460, corrected errors 3.8, 2.9 (yellow box, green font) provide evidence that corrections in that range are possible. For Ramos and Wbc, corrections yield optimum rendering at 0.9 (Q4 CDC) and 1.3 (Q3 CDC), respectively. These results show a mean 1.3 pixel shift is correctable, but not consistently above ≥ 1.8. Thus, a systematic solution to correct chromatic distortion up to ∼3.8 pixel shift is feasible if a metrology grid employs multi-site corrections.

6. RENDERED SPECTRAL OBJECTS

Average intensity spectra $\langle I(\lambda_j)\rangle$ include stationary contributions from a common Xe-arc lamp source and optics (Fig. 17, left). The camera A group Rbc, Wbc, Jur (solid lines) share a similar spectral response with relatively small mean variation. Camera B spectra show variations among A549, H460, H1975, Ramos, due either to a change in detector spectral response between sample measurements or differences in cell-type scattering. Averages are removed from covariance relative intensity fluctuations. Matrix elements are shown with root relative covariance values $c_{ij} = |\langle \delta i(\lambda_j) \cdot \delta i(\lambda_k)\rangle / (\langle I(\lambda_j)\rangle \langle I(\lambda_k)\rangle)|^{1/2}$ in Fig. 17 (right). The Jur and Wbc covariance elements are distinct and larger than the other rendered object populations. However, a complete identification of objects among multiple populations requires classification outside this paper's scope.

A pixel sort renders spatially localized spectral objects. BF and DF images with 3–39 [μm] object size distributions are shown in Fig. 18; 217 objects are rendered from seven cell populations. Blob decomposition is one method that can be used to further

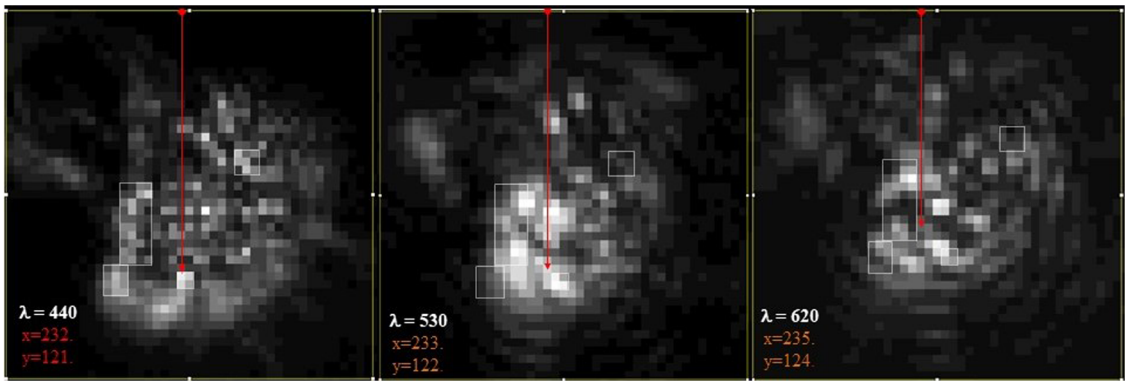

Fig. 15. Wavelength-dependent translation and contrast changes for an H460 cell. Four boxes enclose an extended object sufficient to measure the positional shift with change of image contrast. The red arrow points to a fixed positional coordinate ($x = 232$, $y = 121$). Chromatic distortion measurements over 11 dimensions yield a 1.5 [pixel] mean shift.

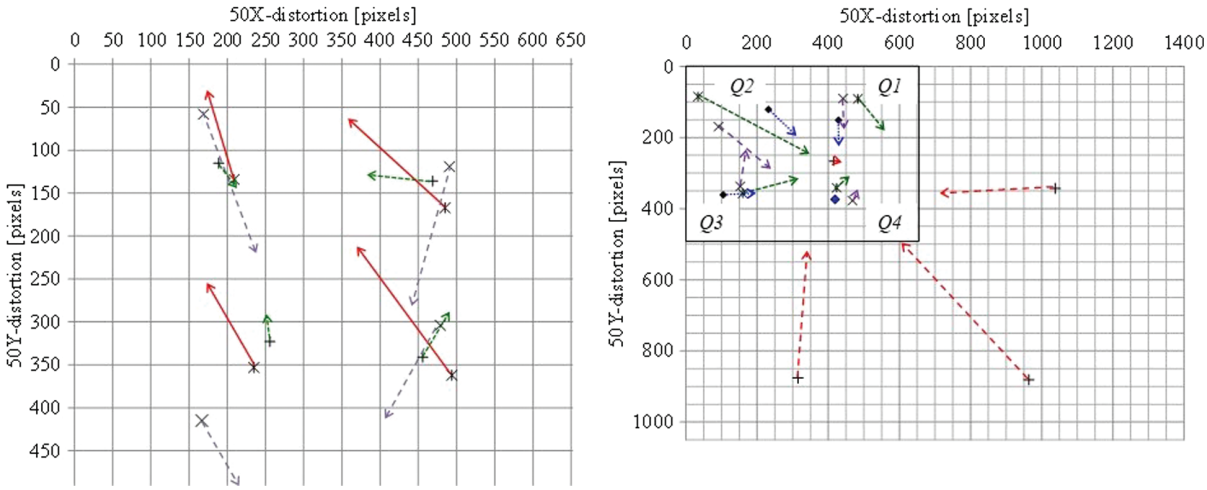

Fig. 16. (Left) Chromatic distortion for three slides using camera A. An error vector origin marks a measurement site with magnitude plotted at 50×. The random orientation of the distortion vectors within a single quadrant shows slide-to-slide variation is greater than systematic optical chromatic distortion. (Right) Chromatic distortions for four slides in camera B with 1392(x), 1040(y) pixel FOV and cropped low distortion region.

Table 3. Chromatic Distortion Mean Shifts[a]

Cell type	A549 - 10x76.9	H460 - 10x77.2	H1975- 10x79.0	Ramos- 29x0.25	Jurkat - 0x1.88	Rbc - 248x1.0	Wbc- 0x2.27
0cdc	0	0.0	0.0	0.0	0.0	0.0	0.0
Q1cdc	3.8	2.3	2.7	1.7	5.2	5.6	2.4
Q2cdc	10.7	3.7	6.0	2.8	5.5	4.4	1.6
Q3cdc	5.1	2.9	3.9	3.8	5.0	4.7	1.3
Q4cdc	1.9	0.0	1.8	0.9	2.7	4.1	2.0

[a]Pixel shifts in boxes result in the maximum rendering per cell type. Single site corrections are effective for ≤ 1.3 pixel shifts; mixed results occur in the error range 1.8–3.8, and are ineffective >3.8.

decompose cell clusters such as found in the Rbc population if required [13].

7. CONCLUSION

Objects of interest are rendered from spectral microscope images under various illumination, detection, and chromatic distortion conditions. Training samples transformed to a binary decision ensemble discriminate intensity vectors in a FOV. Sample-dependent parameters produce binary decisions without other transformation heuristics. Excluded middle binary decisions remove order-dependent errors when multisets occur at minimum error biases. A global bias maximizes object number and size in the presence of non-sample related signals. As a result, sample size is adjusted to optimize accuracy with lower limits determined by measurement dimensionality and sample

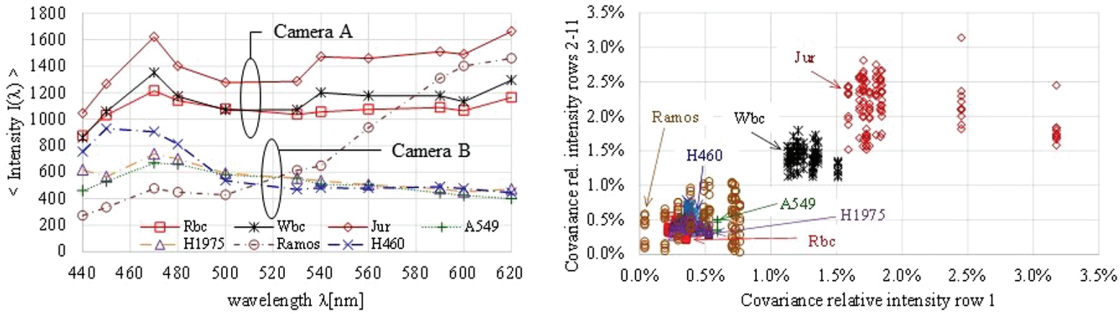

Fig. 17. Intensity characteristics for rendered objects of the seven cell types. (Left) Average intensity spectra $\langle I(\lambda_i)\rangle$ from 440–620 [nm], camera 1 (solid), camera 2 (dashed). (Right) Root relative covariance c_{ij} per cell type.

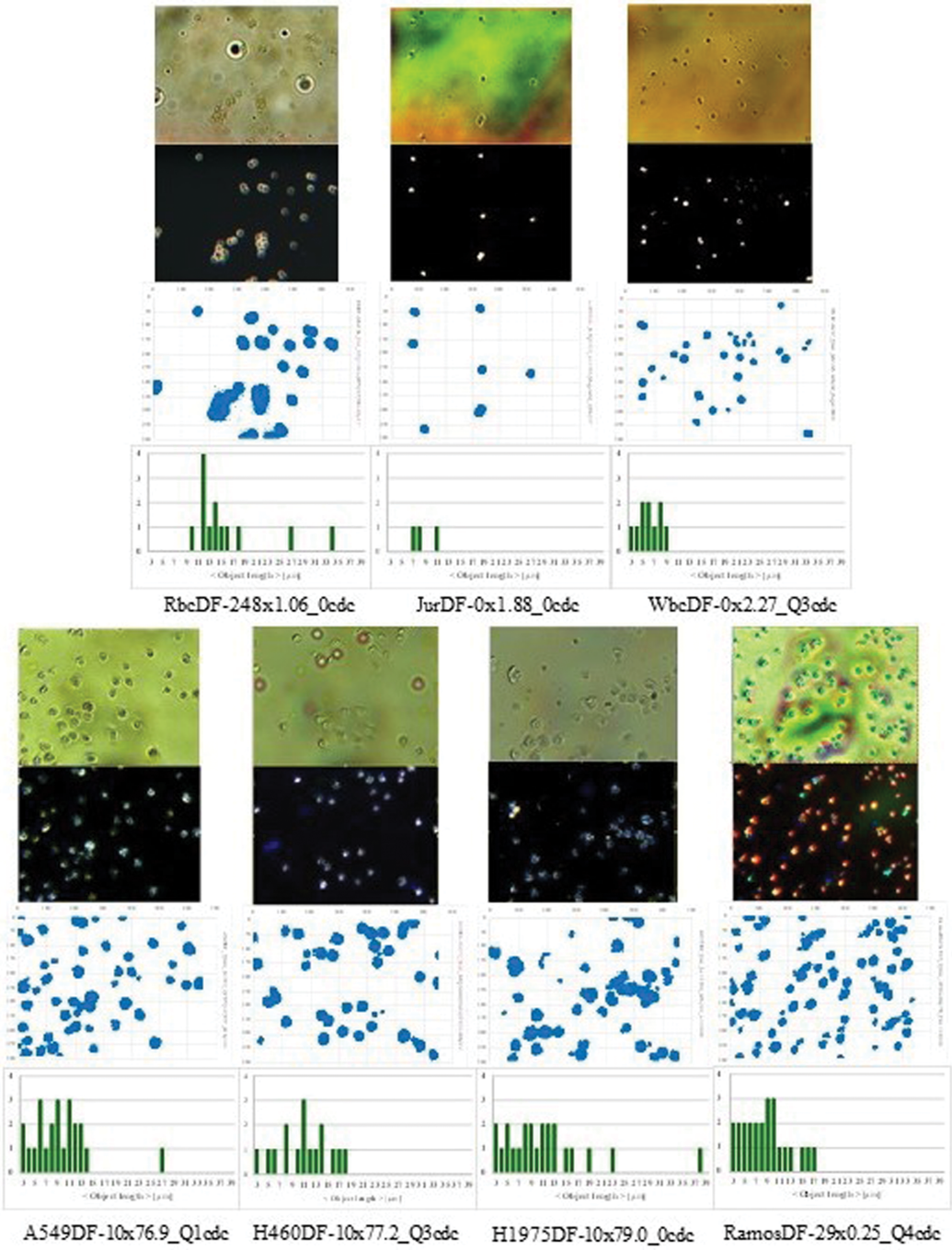

Fig. 18. Spectral images of seven cell types (columns): Rbc, Jur, Wbc, A549, H460, H1975, Ramos, and (rows): bright and dark fields, rendered objects, and 3–39 [μm] size distributions.

covariance stability. Seven blood and cancer cell populations with size distributions from 3–39 μm are rendered to 217 spectral objects. CDC is feasible but single site calibration is not sufficient. The algorithm minimizes optics errors and renders spectral objects suitable for classification.

Disclosures. The authors declare no conflicts of interest.

Data availability. Data underlying the results presented in this paper are not publicly available at this time but may be obtained from the authors upon reasonable request.

REFERENCES

1. M. Gesley and R. Puri, "A high throughput spectral image microscopy system," Rev. Sci. Instrum. **89**, 013705 (2018).
2. M. Gesley, R. Goldsby, S. Lane, and R. Puri, "Spectral image microscopy for label-free blood and cancer cell identification," Proc. SPIE **10890**, 58–73 (2019).
3. "ATCC Number: CRL-5908," 2022, http://www.atcc.org/.
4. R. Fisher, "The use of multiple measurements in taxonomic problems," Ann. Eugenics **7**, 179–188 (1936).
5. F. Rosenblatt, *Principles of Neurodynamics* (Spartan Books, 1962).
6. N. Cristianini and J. Shawe-Taylor, *Support Vector Machines* (Cambridge University, 2000).
7. K. Fukunaga, *Introduction to Statistical Pattern Recognition*, 2nd ed. (Academic, 1990).
8. Y. LeCun, Y. Bengio, and G. Hinton, "Deep learning," Nature **521**, 436–444 (2015).
9. R. Rojas, *Neural Networks–A Systematic Introduction* (Springer-Verlag, 1996).
10. T. Hastie, R. Tibshirani, and J. Friedman, *The Elements of Statistical Learning*, 2nd ed. (Springer, 2009).
11. E. Strickland, "Andrew Ng: unbiggen AI," IEEE Spectrum (2022) https://spectrum.ieee.org/andrew-ng-data-centric-ai.
12. A. Lee, B. Nadler, and L. Wasserman, "Treelets–an adaptive multi-scale basis for sparse unordered data," Ann. Appl. Statistics **2**, 435–471 (2008).
13. T. Lindeberg, "Scale selection properties of generalized scale-space interest point detectors," J. Math. Imaging Vis. **46**, 177–210 (2013).